Journal of the Korean Society of Oceanography
Vol. 34, No. 2, pp. 59—72, June 1999

Characteristics of Southern Ocean Sea Ice Distribution Modeled Using Cavitating Fluid Rheology and Climatological Atmospheric Data

HYUNGMOH YIH AND CARLOS R. MECHOSO[1]
Korea Inter-University Institute of Ocean Science, Pukyong National University, Pusan 608-737, Korea
[1]Department of Atmospheric Sciences, University of California, Los Angeles, CA 90024, U.S.A.

Cavitating fluid sea ice model of Flato and Hibler (1992) is applied to the Southern Ocean with an idealized, circular Antarctica. Using climatological atmospheric forcing fields averaged in the zonal direction, we show that oceanic heat flux and ice velocity have major effects on the seasonal change of ice edge, as other studies showed. In our model results, there appears a zone of free drift that contains a polynya zone. Thermodynamic forcing functions make dominant contributions to daily increments of ice thickness and compactness, except the zones of ice edge and polynya. The dominant contributions are also shown in distributions of the temperature on ice surface and several terms in surface heat balance equation, and are also confirmed by those obtained from the thermodynamic-only model with the different locations of ice edge.

INTRODUCTION

Recognizing the increase of atmospheric greenhouse-gas concentrations led to possible scenarios for global climate change. The scenarios stimulated studies of climate-component media and their relationships. As a part of the studies, understanding changes of sea ice characteristics gained new significance, because the sea ice changes might indicate the effect of global warming due to the increase of atmospheric greenhouse-gas concentrations and are expected to influence the global conveyor-belt-circulation through deep-water formation.

Large-scale sea ice models consist of dynamic and thermodynamic parts. Several dynamic models were introduced to understand long-term mean motion of sea ice mainly in the Arctic Ocean. Fel'zenbaum (1958) introduced the free-drift model which does not have the internal ice interaction in the momentum balance. Newtonian viscous interaction was considered by Campbell (1965). Rothrock (1975) calculated the steady drift with the assumption of incomperssible sea ice. Hibler (1979) used a viscous-plastic rheology which relates ice deformation and thickness to internal stress to ice cover. For thermodynamic models, Maykut and Untersteiner (1971) developed a time-dependent model for multi-year sea ice, and Semtner (1976) adopted their model in three-dimensional simulations with some modifications. Coupled dynamic and thermodynamic sea ice models were used to carry out long-term equilibrium simulation of ice cover in polar oceans (Hibler, 1979; Parkinson and Washington, 1979; Stoessel *et al.*, 1990).

Though the viscous-plastic rheology developed by Hibler (1979) was evaluated as the best representation of sea ice dynamics in large-scale models by the Sea Ice Model Intercomparison Project (Lemke *et al.*, 1997) for the Arctic Ocean, Flato and Hibler (1992) presented a simpler dynamic model of sea ice. Their model uses cavitating fluid rheology that captures a dominant characteristic of sea ice interaction, i.e., strength in compression and relative weakness in tension. They showed that realistic patterns of ice transport were obtained in the simulation of Arctic ice cover, and that results were similar to those obtained by the more-complicated model of Hibler (1979). Their model was considered as a candidate for improving the computational efficiency of sea ice component in coupled general circulation models of sea ice and ocean (Meehl, 1992; Semtner and Chervin, 1992). The cavitating fluid rheology also allows pure free-drift expansion of sea ice when ice flow is divergent. Free drifts of sea-ice buoys were observed in the Weddell Sea (Martinson and Wamser, 1990; Kottmeier *et al.*, 1992; Vihma and Launiainen, 1993; Kottmeier and Sellman, 1996). The computational efficiency and observational facts motivated us to choose the Flato and Hibler's (1992) model for the

climatological study of ice distribution especially in the Southern Ocean.

Our objective is to document the performance of Flato and Hibler's (1992) model in the Southern Ocean in response to a set of atmospheric forcing fields. In following sections, after briefly describing the Flato and Hibler's (1992) model and three modifications we made, we explain model results of control run and the evolution of thermodynamic variables. Summary of results and discussion are in the final section.

DESCRIPTION OF THE FLATO AND HIBLER'S (1992) MODEL

The model consists of momentum and continuity equations. The momentum equation is to get ice velocity and the continuity equations are for temporal changes of thermodynamic variables, i.e., ice thickness and compactness. Readers are referred to Flato and Hibler (1992) and Hibler (1980) for the complete model description including parameter values.

Momentum balance

The momentum balance is expressed as the following equation, which is among the Coriolis force, forces due to air and water stresses, and forces due to slope of sea surface and internal ice interaction.

$$-mf\hat{k}\times\vec{u}+\vec{\tau}_a+\vec{\tau}_w-mg\nabla D+\vec{F}=0 \qquad (1)$$

where m ($=\rho_i h$) is the mass of sea ice, ρ_i is the ice density, and h is the ice thickness, f is the Coriolis parameter, $\hat{k}$ is the vertical unit vector, $\vec{u}$ is the ice velocity, $\vec{\tau}_a(\vec{\tau}_w)$ is the stress force due to air (water) drag, g is the gravitational acceleration, D is the sea-surface dynamic height, and the force $\vec{F}$ is due to variation in internal stress. The stress forces are given by the following quadratic formulation (McPhee, 1975).

$$\vec{\tau}_a=\rho_a C_a \mid \vec{U}_a \mid [\vec{U}_a\cos\phi+\vec{U}_a\sin\phi] \qquad (2)$$

$$\vec{\tau}_w=\rho_w C_w \mid \vec{U}_w-\vec{u} \mid [(\vec{U}_w-\vec{u})\cos\theta+(\vec{U}_w-\vec{u})\sin\theta] \qquad (3)$$

In the above formulation, $\vec{U}_a(\vec{U}_w)$ is for the geostrophic wind (ocean-current) velocity, $C_a(C_w)$ wind(water)-drag coefficient, and $\phi(\theta)$ is wind (water) turning angle which is fixed to $-25°$ in this paper. It is assumed that the force $\vec{F}$ is dependent only on the internal ice pressure p, i.e. $\vec{F}=-\nabla p$. The ice interaction is included in ice rheology through the scheme of cavitating fluid correction for internal pressure and ice velocity. The scheme of cavitating fluid correction is expressed as follows using parameterized compressive strength p_{max}.

(a) $p\cong 0$, if $\nabla\cdot\vec{u}\geq 0$,
(b) $0\leq p\leq p_{max}$, if $\nabla\cdot\vec{u}=0$, and
(c) $p=p_{max}$, if $\nabla\cdot\vec{u}\leq 0$ (4)

The compressive strength is parameterized as $p_{max}=p^*h\cdot\exp\{-K(1-A)\}$, where p^* and K are empirical constants. Ice compactness A represents the fraction of ice-covered area, whose range is $0\leq A\leq 1$.

To find the ice velocity, the free-drift velocity is calculated in the first step, which is the ice velocity with no ice interaction, i.e., p=0. While applying the cavitating fluid corrections with respect to the range of pressure as the second step, iterations continue until differences between pressures obtained in consecutive iteration steps are smaller than the tolerance limit specified. Corrected velocities are obtained by solving the pressure correction equation.

Following three modifications are made to the original code of Flato and Hibler (1992). The first one is the direct calculation of free-drift velocities from the stress forces. The second one is that the f-plane approximation is not used because of the winter extent of sea ice in the Southern Ocean. The last one is that the tolerance limit is applied with respect to the consecutive velocity differences instead of the consecutive pressure differences.

Evolution of the thermodynamic variables

Temporal changes of the thermodynamic variables are due to both flux divergences and thermodynamic forcing functions. The divergence terms utilize the ice speeds obtained from the momentum equation. The thermodynamic forcing functions are expressed in terms of thermodynamic growth rates obtained by a two-level thermodynamic model of sea ice (Hibler, 1980). The two levels of thick and thin ices are divided by demarcation thickness h_o, and they have compactness A and $(1-A)$, respectively. The demarcation thickness is chosen to be small compared to mean ice thickness but large enough so that heat fluxes through h_o-thick ice are substantially less than those through open water. Also used are a model for heat conduction through

sea ice and a basic surface heat balance model.

The temporal changes are expressed by following continuity equations.

$$\frac{\partial h}{\partial t} = -\nabla \cdot (\vec{u} h) + S_h,$$
$$\text{where } S_h = (1-A) \cdot f(0) + A \cdot f(h/A) \quad (5)$$
$$\frac{\partial A}{\partial t} = -\nabla \cdot (\vec{u} A) + S_A,$$
$$\text{where } S_A = \frac{f(0)}{h_0} \cdot (1-A) \cdot H_V [f(0)] + \frac{A}{2h} \cdot S_h \cdot H[-S_h] \quad (6)$$

Thermodynamic forcing functions, S_h and S_A, represent the total growth rate of thickness and total rate of change of ice-covered area due to melting or freezing, respectively. H_V is the Heaviside unit step function. Thermodynamic growth rates, $f(h/A)$ and $f(0)$, are for thick and thin ices, respectively. The growth rates are estimated, at the bottom of sea ice, from the balance between the heat conduction through the ice and the oceanic heat flux, F_w, supplied to the mixed layer fixed to be 60 m thick in time and space. That is,

$$f(h) = \frac{1}{\rho_I L}(F_{CON} - F_w) = \frac{1}{\rho_I L} \cdot \frac{K}{h}(T_B - T_o - F_W) \quad (7)$$

where L is the latent heat of fusion and $F_{CON}\{=\frac{K}{h}(T_B - T_o)\}$ is heat conduction through ice, T_B is the temperature at ice bottom (fixed to 271.2 K), T_o is the temperature on ice surface, and K is the ice conductivity. When calculating heat conduction through ice, ice thickness of 0.05 m is used for thinner ice than that.

The temperature on ice surface, T_o, is calculated from the basic surface heat balance equation by Newton-Raphson method. If T_o is greater than 273.16 K, it is set equal to 273.16 K. If there is some imbalance of surface flux, the imbalance is used to melt sea ice.

$$(1-\alpha)F_{SHO} + F_{LON} + F_{SEN} + F_{LAT} - F_{BAC} + F_{CON} = 0 \quad (8)$$

where α is the surface albedo, F_{SHO} is the incoming short-wave radiation, F_{LON} is the incoming long-wave radiation. The bulk sensible and latent heat fluxes, F_{SEN} and F_{LAT}, and back radiation, F_{BAC}, are given as follows. $F_{SEN} = D_1 |\vec{U_a}| (T_a - T_o)$, $F_{LAT} = D_2 |\vec{U_a}| [q_a(T_a) - q_s(T_o)]$, and $F_{BAC} = -D_3 T_o^4$, where the constants D_1 and D_2 are bulk sensible and latent heat transfer coefficients, T_a is the air temperature, q_a and q_s are specific humidities at the reference level and the ice surface, and the constant D_3 is the Stefan-Boltzman constant times the surface emissivity.

SEA ICE MODEL RESULTS ADJUSTED CLOSE TO THE OBSERVED STATE

The purpose of this section is to find out roles of ice dynamics and oceanic heat flux supplied to the mixed layer in choosing a control run. The control run is chosen as one with the northern limit of sea ice extent most close to observed states in the zonally symmetric sense, when model states are in statistical equilibria. Examples of such observed states are found in Zwally *et al.* (1979, 1983), Gordon (1981), and Gloersen *et al.* (1992). They showed that the minimum extent usually occurred in or around February, and that the maximum in or around September. Characteristics of model results in the control run are also discussed.

The model resolution is 2° in latitude by 10° in longitude. The time step of integration is one day. Range of the model domain is from 70° S to the latitude of 50° S. At the initial time ice thickness and compactness decrease linearly from 1.5 m and 1.0 at the southern boundary to 0 m and 0.0 at the 64° S latitude, respectively. There is initially no ice north to the latitude of 64° S. The tolerance limit of 10^{-5} is specified to the consecutive difference of velocity field. In the thermodynamic part, the demarcation thickness of 1 m is used as in other studies, e.g., Ackley *et al.* (1980) and Stoessel *et al.* (1990).

In this study, the ocean is assumed to be at rest. Atmospheric forcing fields consist of geostrophic wind velocity, surface air and dew point temperatures, and incoming long-wave and short-wave radiations. The forcing fields are space-and-time series which are climatological ones averaged in the zonal direction. In accordance with the averaged forcing fields, the Antarctic coastline is idealized as that of a circular Antarctica.

Seasonal values for geostrophic wind velocity and incoming short-wave radiation are from Jenne *et al.* (1971) and Sasamori *et al.* (1972), respectively. The atlas data of Taljaard *et al.* (1969) are for surface air and dew point temperatures. Incoming long-wave radiation is calculated from the surface air temperature, as was done by Parkinson

and Washington (1979). All the fields are linearly interpolated to daily values. Outgoing long-wave radiation is calculated in the ice model at every time step. The same atmospheric forcing fields were used in several studies for sea ice simulation in the Southern Ocean (Parkinson and Washington, 1979; Gordon, 1981; Stoessel *et al.*, 1990)

Our results can be treated as spatially one-dimensional ice characteristics in the Southern Ocean, which are symmetric in the zonal direction and change in time and meridional direction. The idealized, circular Antarctica and atmospheric forcing functions zonally averaged are adopted based on results of Hyde *et al.* (1990) and Stoessel *et al.* (1990). Hyde *et al.* (1990) showed the ice and snow fields modeled by a nonlinear seasonal energy balance model. Their modeled sea-ice boundaries are approximately circular and close to the observed boundary of Antarctic sea ice distribution by the Electrically Scanning Microwave Radiometer (ESMR) in January and July (Zwally *et al.*, 1983). The similar circular distribution pattern was also presented by Stoessel *et al.* (1990).

Fig. 1 shows space-time series, over the sub-domain of 56-70° S, of four atmospheric forcing fields. Meridional components of geostrophic wind velocity are zero over the sub-domain (not shown). The distribution of short-wave radiation shows a distinct seasonal pattern with contours crowded during the austral summer. Zonal components of geostrophic wind velocity in the middle of October show the southward shift of all contours. Patterns of

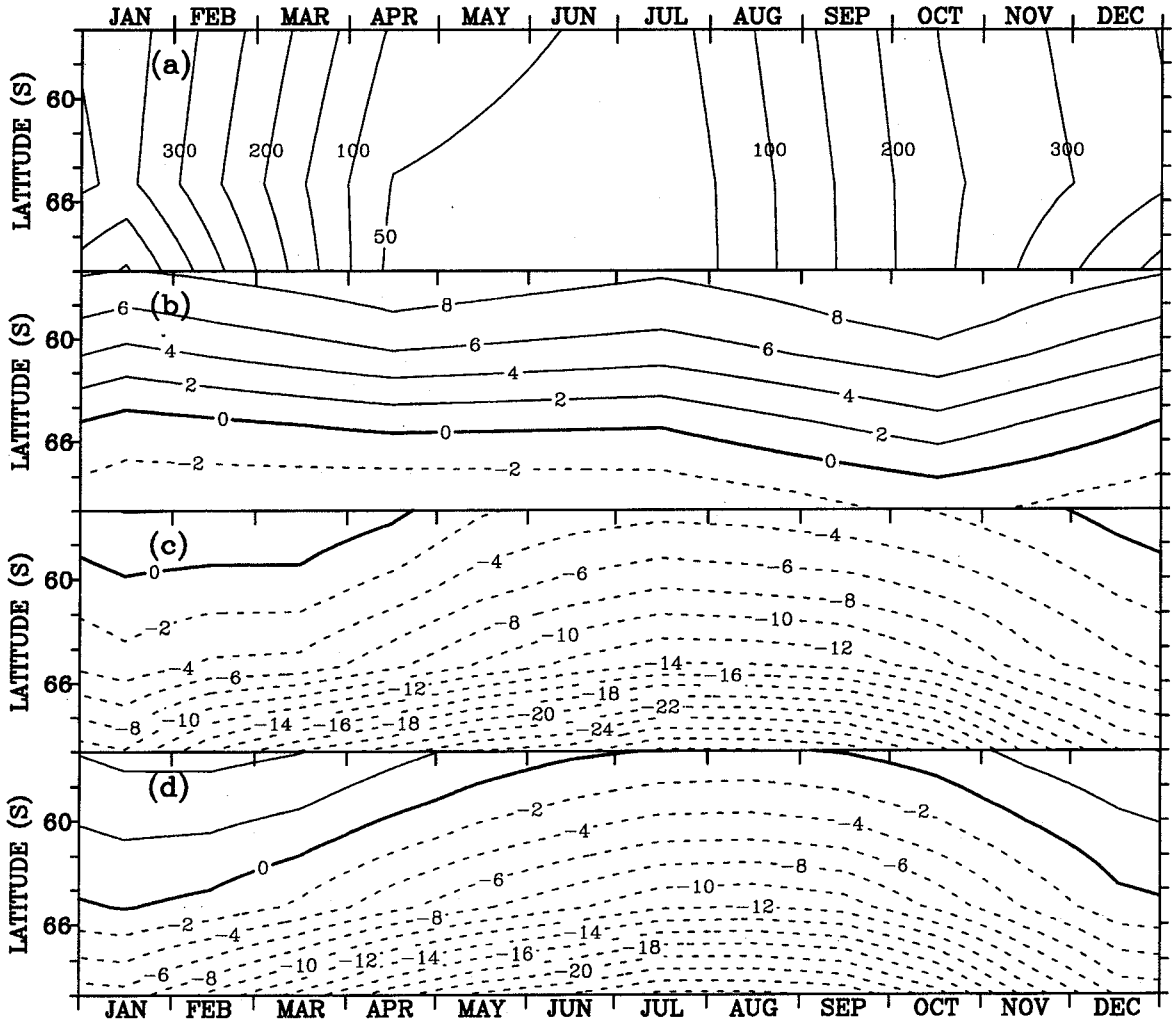

Fig. 1. Atmospheric forcing fields are contoured on the phase plane of time and latitude. Shown are (a) incoming short-wave radiation, (b) geostrophic wind speed in the zonal direction, and (c) dew point and (d) surface air temperatures. Meridional component of geostrophic wind is not shown, because they are all zero in the latitudinal range. Hereafter, dashed contours are used for negative values.

air and dew point temperatures are approximately opposite to that of the zonal component of the wind velocity. Thus, atmospheric forcing fields reveal seasonal changes well.

We applied the atmospheric forcing fields to the ice model for nine model years. Among four model runs performed, three runs are with the full model with different oceanic heat fluxes of 13, 6.5, and 0 Wm^{-2} to the mixed layer. The remaining one is the thermodynamic-only model run with oceanic heat flux of 6.5 Wm^{-2}. All model results are observed to be in the state of statistical equilibrium in Year 6. There is no climate drift observed. We define each season as the period during which the ice edge remains on the same latitude. From now on, the adjective of austral will not be used while mentioning each reason.

In Fig. 2, latitudinal changes of ice edges during Years 1 and 6 are shown using thin and thick lines, respectively. Let us compare results of the full model runs first. Ice-covered period is decreased with increasing oceanic heat flux, as the model approaches the state of statistical equilibrium. The decreased period is due to the ice growth rate $f(h)$ in (7) which works as a control factor in the thermodynamic forcing function to the temporal rate of change of the compactness in (6). Minimum retreats during austral summer are not observed in the full model runs with $F=13$ and 0.0 Wm^{-2}. The case shown in Fig. 2d is an extreme case of no heat supply to the mixed layer. Only the results obtained from the full model run with $F_w=6.5\ Wm^{-2}$ (Fig. 2b) show the similar appearance of maximum and minimum extents to the observed mentioned above,

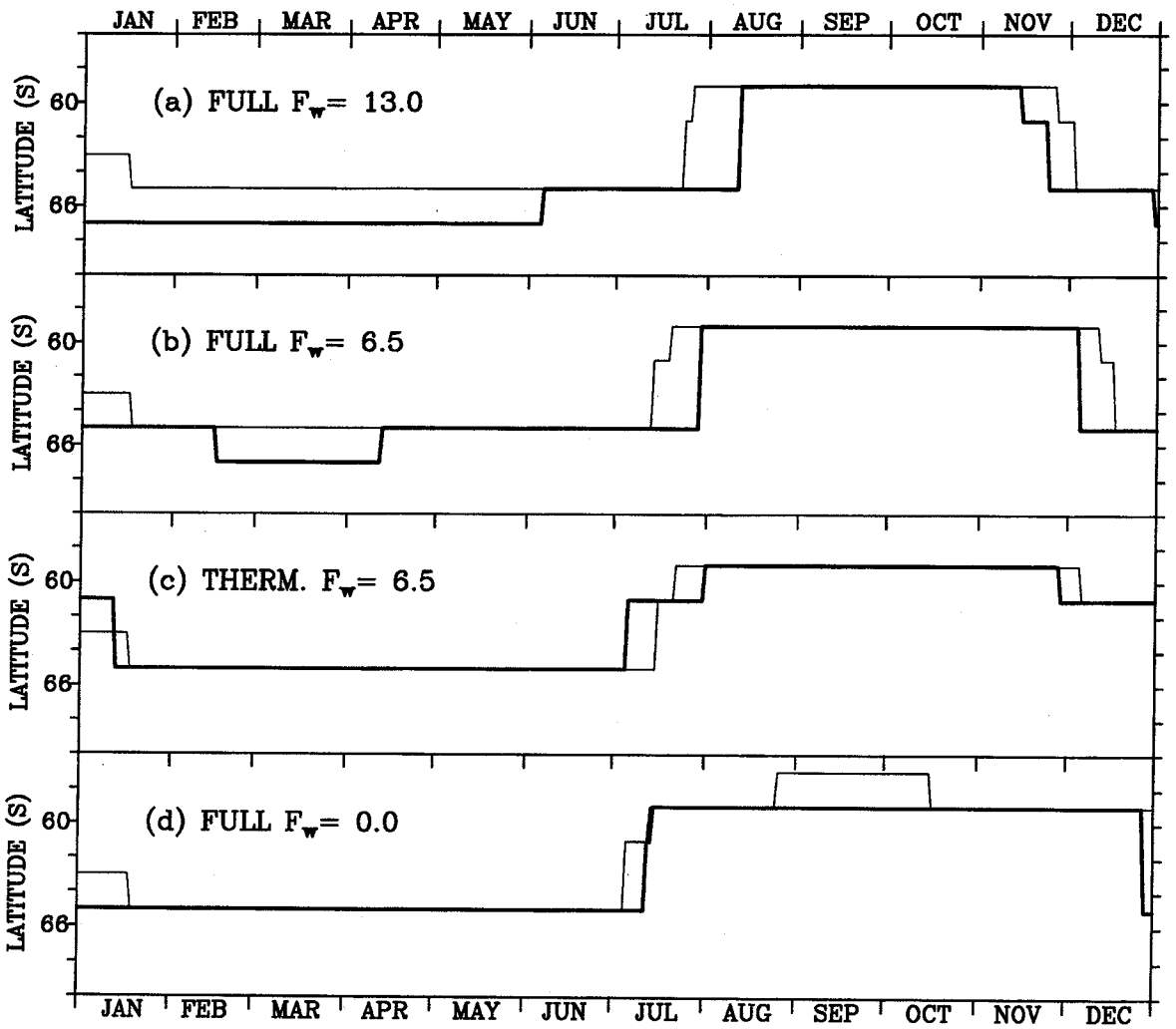

Fig. 2. Plots for the change of ice edges during Years 1 and 6 for three different heat fluxes of (a) 13, (b) and (c) 6.5, and (d) 0 Wm^{-2}. Thin (thick) line is used for Year 1 (6). Results shown are obtained from the full model, except those on the third frame from the top, i.e., Fig. 2c which is obtained from the thermodynamic-only model.

though there are some phase shifts. The phase shifts could be due to the forcing fields averaged in the zonal direction. Thus, we take the case with $F_W = 6.5$ Wm^{-2} as the control run.

The thermodynamic-only case shows the effect of not including the dynamic part (Fig. 2c). The effect appears as the longer duration of ice presence during winter and further advance of the ice edge to the north during summer than those in the case of the control run. Due to the further advance appeared, the minimum extent of ice coverage has disappeared during summer. Based on compared results, seasonal change in sea ice coverage owes to both the ice motion and oceanic heat flux. Further comparison in detail will be shown when we consider evolutions of the thermodynamic variables.

In order to describe the characteristics of the state of statistical equilibrium, we will use distributions of ice variables obtained from the control run during Year 6. As shown Fig. 3a, during seasons other than

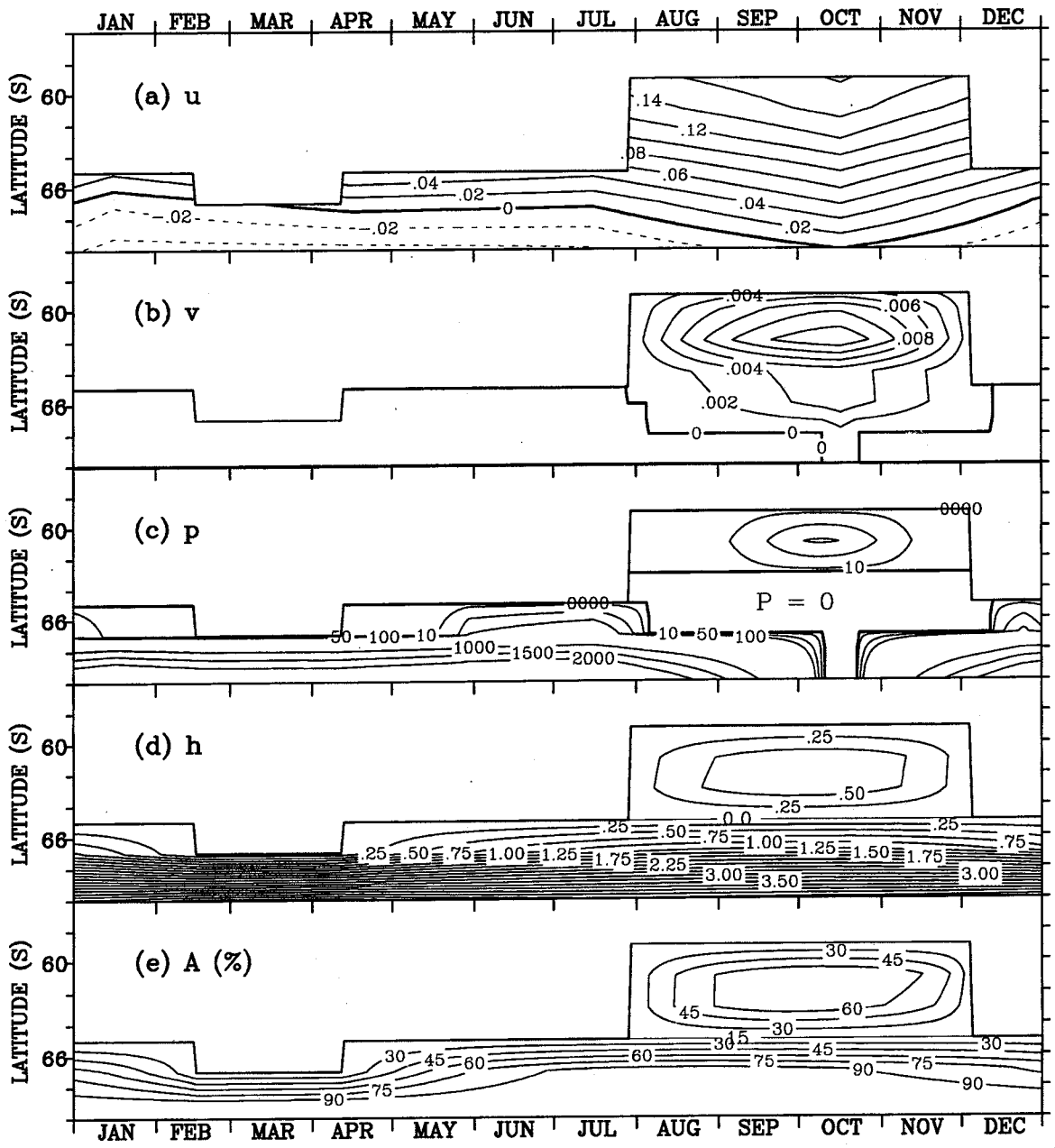

Fig. 3. Distributions of (a) zonal ice speed, (b) meridional ice speed, (c) internal pressure, (d) ice thickness, and (e) compactness. These are obtained from the full model with the oceanic heat flux of 6.5 Wm^{-2}, on the time and latitude plane during Year 6.

winter, sea ice is present in the region where easterly winds blow. However, effects of nonlinearity, including the stress forces, the cavitating fluid correction, and thermodynamic processes, appear as two different directions of zonal ice speed. During winter season, dipped signals appear in zonal ice speeds as appeared in the wind speed in the same direction, though the dipped ice signals are slightly shifted to the south. The distribution of meridional ice speed shows a core of fast meridional speed along the 62° S latitude and diverging zone around zero contour (Fig. 3b). Around the diverging zone, there appears a region of free drift with zero internal pressure, which corresponds with the case (a) in (4) (Fig. 3c). It is also noticeable during winter season that both the zero contour of thickness and contour with the lowest limit of compactness, i.e., $A=15\%$, separate the advanced zone of sea ice from the permanent zone of ice (Figs. 3d and 3e). We call the area surrounding the separating contour lines the zone of polynya. The distribution of compactness is similar to that of ice thickness, except the period and region possibly affected by the nonlinear constraint of the compactness.

EVOLUTION OF THE THERMODYNAMIC FIELDS

The polynya found in the previous section is not the latent heat polynya observed usually along coasts, islands, or big icebergs. Though the polynya was appeared in the open ocean area, that does not belong to the sensible heat polynya maintained by the upwelling of relative warm water to the sea surface (Comiso and Gordon, 1998). This ice model is not coupled to ocean model. There is no upwelling mechanism included in. In order to show mechanism for appearance and disappearance of the polynya zone, we will investigate fields of daily increments, divergences, and forcing functions of thermodynamic ice variables. Attention will be also paid to changes of the thermodynamic fields in relation to atmospheric heat fluxes into the ice, temperature on ice surface, and heat conduction through the ice.

Fig. 4 shows distributions of three terms in the continuity equation of ice thickness, i.e., (5), and percentage distributions of two term on the right-hand side. There are several zero nodal-lines in the latitudinal distribution of daily increment of the thickness, $h(t+1)-h(t)$ (Fig. 4a). The straight nodal line in the polynya zone corresponds to the zero-contour of ice thickness located along the latitude of 65° S shown in Fig. 3d. There is also a group of three nodal lines along the southern boundary. Contours in the zone of permanent ice during spring to fall are roughly anti-symmetric with respect to the nodal line appeared in early March. However, during winter, the nodal line appears with the shape of number 3. Contours appeared in winter season show also roughly anti-symmetric pattern with respect to a time-line corresponding to mid-October. Contours in the advanced zone indicate that freezing and melting processes are taken place on two boundaries of the advanced zone, i.e., ice-edge lines representing the rapid change of season. Melting and freezing patterns in the permanent zone are similar to those appeared in the advanced zone, except the duration of their occurrence. Processes of melting and freezing appeared in the two zones as well as the presence of the ploynya zone make the shape of number 3 appeared during winter.

Let us find out contributions of dynamic and thermodynamic parts to the daily increment. The divergence field of thickness flux is positive except both during one month from the mid-March to mid-April near the southern boundary and regimes represented by many small cells with the shape of needle (Fig. 4b). Large values of positive divergence appear along sea ice edge and in the polynya zone during the period of mid-summer to mid-winter. The thermodynamic forcing field shows very similar pattern to both the field of daily increment of thickness mainly for negative contours appeared from the late winter to the end of spring and the group of three nodal lines along the southern boundary (Fig. 4c). Thus, the thermodynamic forcing dominates the daily increment of thickness in the melting phase, but the divergence field mainly affects the daily increment along the ice edge and the polynya zone in the freezing phase.

Percentage distributions of the two functions are shown to figure out their relative contributions to the daily increment of thickness (Figs. 4d and 4e). In the two figures, if one forcing shows negative percentage, the total percentage of 100% is obtained by adding its absolute value to the other. It is recognized in Fig. 4d that the contour with negative percentage works as the positive forcing to daily increment. Along the sea ice edge and central line of the polynya zone, the two terms balance each other, except short periods (Figs. 4d and 4e). Along

ice edge, crowded contours of divergence of thickness flux last from 16 to 19 in September with its maximum of 70% (Fig. 4d). Those of thermodynamic forcing with negative percentages last from 18 to 21 in September with their minimum of −70% (Fig. 4e). In the polynya zone, the two functions offset each other except following two periods. One period is from 21 to 23 in October with the dominant contribution by the divergence field. The other period is from 24 to 25 in October with the dominant contribution by the thermodynamic forcing field. As percentage distributions indicate in Fig. 4e, the domination of the thermodynamic forcing (>90%) is confirmed again, excluding sea ice edge in early winter (e.g., 16−19 in September), the polynya zone from 21 to 23 in October, and the small cells. The small cells appear as signals of forcing with opposite sign to that of surrounding

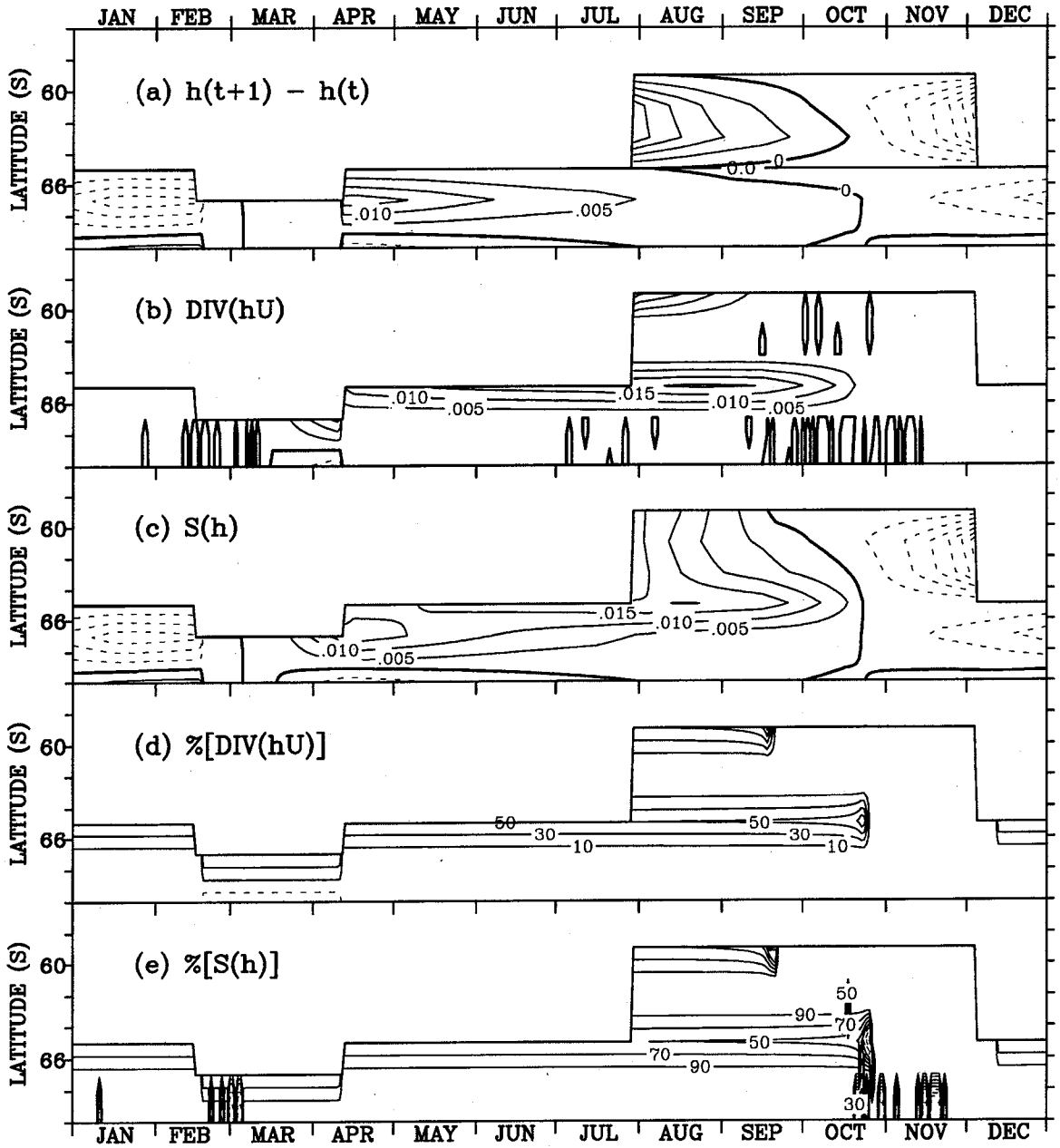

Fig. 4. Same as Fig. 3, except for (a) distributions of daily increment of the thickness, (b) divergence of thickness flux, $\nabla \cdot (\vec{u}h)$, (c) thermodynamic forcing function, S_h, for the thickness, (d) percentages of the divergence, and (e) percentages of the thermodynamic forcing function. The sign convention explained in the text is to make sum of two percentages 100%. For the percentage distributions, contoured values with interval of 20 are $\pm(10, \cdots, 90)$, and zero contour is not included to avoid complexity. In other frames, thick solid-contour is used for zero value.

regime of period and latitudes. In the excluded zones, the divergence comes in first, and then the thermodynamic forcing follows. This switching could be treated as a representative for the phase change from the freezing to melting. An additional point found is that the interior of the advanced zone around the latitude of 62° S is also forced dominantly by the thermodynamic forcing.

The daily increment of compactness also shows a nodal line with its shape similar to that of number 3 (Fig. 5a). There are also nodal lines along the latitude line of 69° S with the long duration for the second one. Large positive increments extend next to ice edge all year long except during winter, which is due to the divergence of compactness flux working as the positive forcing (Fig. 5b). Near the southern boundary, there are many cells of the divergence with the needle shape, also working as the positive forcing, periodically appeared all year long except during summer. Also near the southern

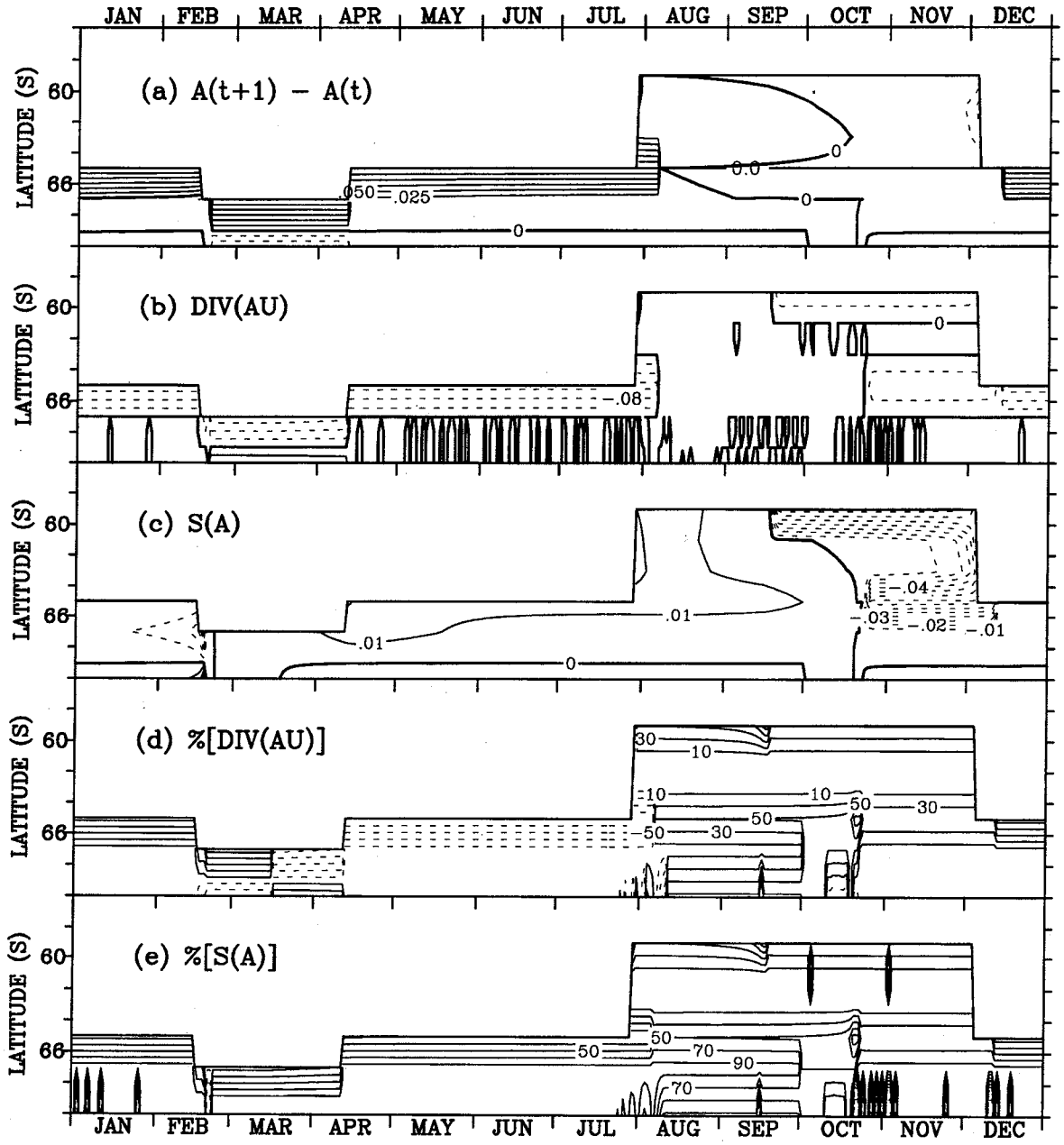

Fig. 5. Same as Fig. 4, except for (a) daily increment of the compactness, (b) divergence compactness flux, $\nabla \cdot (\vec{u}A)$, (c) thermodynamic forcing, S_A, for the compactness, (d) percentages of the divergence, and (e) percentages of the thermodynamic forcing function.

boundary, the group of three nodal lines appears as in the field of daily increment (Fig. 5c). Over the zone of polynya, the two forcing functions offset each other in percentages, as observed in the thickness case, except the dominant contribution by the divergence field reaching 90% during the period of 19 to 23 in October (Figs. 5d and 5e). The thermodynamic forcing also dominates in the zone of permanent ice and in the interior of the advanced zone around the latitade of 62° S (Fig. 5e).

We will further investigate the atmospheric fields to know how forcing functions of ice thickness and compactness have been driven, and then describe the fields obtained from the thermodynamic-only model. Thick and thin ice contribute to the atmospheric heat fluxes with weights of A and $(1-A)$, respectively. Positive heat fluxes is from the atmosphere to the ice surface. Positive flux of sensible heat appears over the region north to the polynya zone during late winter and near the southern boundary during the period of March to May (Fig. 6a). Large loss of sensible heat to the air continues from the time line representing the beginning of winter season to late October over the polynya zone. Sea ice looses latent heat into the air all year long (Fig. 6b). The largest flux of latent heat is appeared mainly in the advanced zone in August and September. Over the polynya zone, latent heat loss is larger in October than other months. During fall, latent heat loss to the air is smaller than any other seasons. In the permanent ice zone, the seasonal change of temperature on ice surface, calculated by

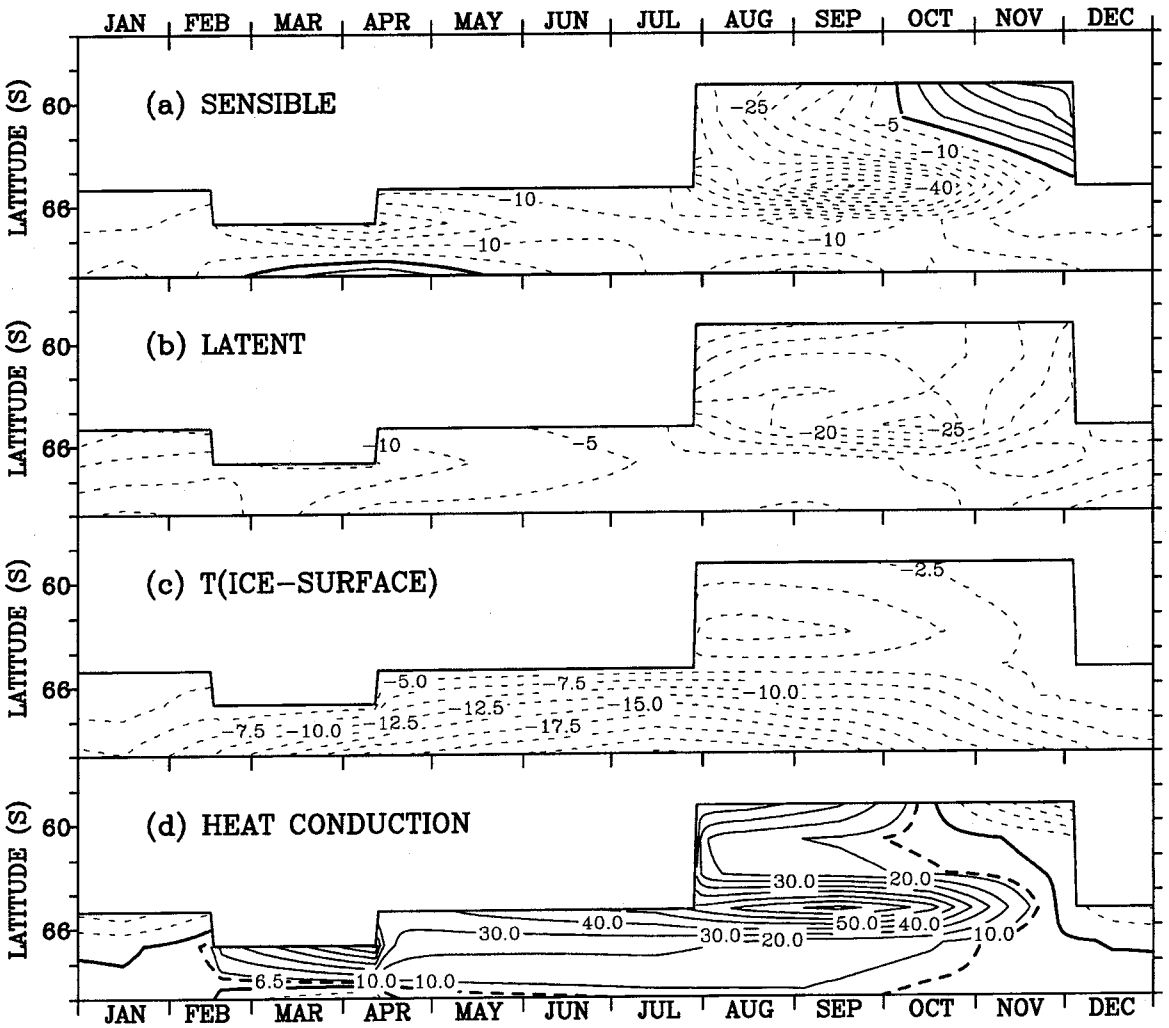

Fig. 6. Distributions of (a) sensible and (b) latent heat fluxes, (c) temperature on ice surface, and (d) heat conduction through ice. These are obtained from the full model with the oceanic heat flux of 6.5 Wm^{-2}, on time and latitude planes during Year 6. The thick dashed contour in Fig. 6d is for the value of 6.5 Wm^{-2} corresponding to the zero grow-rate of sea ice.

(8), shows almost the same pattern as those of air and dew point temperatures shown in Figs 1c and 1d (Fig. 6c). In the advanced zone, the lowest temperature (< -7.5°C) appears during the period of August to mid-September.

The spatial difference of the growth rate in (7) is actually due to the heat conduction determined by the ice thickness and temperature on ice surface. The thick-dashed contour of 6.5 Wm^{-2} indicates the zero growth-rate of sea ice along which there is the heat balance between the heat conduction and the oceanic heat flux (Fig. 6d). Magnitude of heat conduction is always larger near sea ice edges and the polynya zone where the flux divergences show more contribution than other regimes to the daily increment. Similarity to the distribution of heat conduction appears in the distribution of sensible heat flux than that of latent heat flux during summer and winter. The strong sensible heat flux is approximately in phase with the strong heat conduction in the polynya zone. The negative maximum of latent heat flux shows about one month delay with respect to the period of strong heat conduction. This is due to stronger effects of sea surface temperature than the specific humidity in the two fluxes. This also indicates the importance of thermodynamic process as revealed by the temperature on ice surface.

There still remains a question on the role of meridional ice advection which led to the pure divergence of ice velocity and the presence of the polynya zone. In the results obtained from the thermodynamic-only model, if there appears a similar polynya zone to that of the control run, the polynya zone is due to the thermodynamic process. That is, the dynamic part of the sea ice model is crucial only in obtaining the ice edge close to the observed,

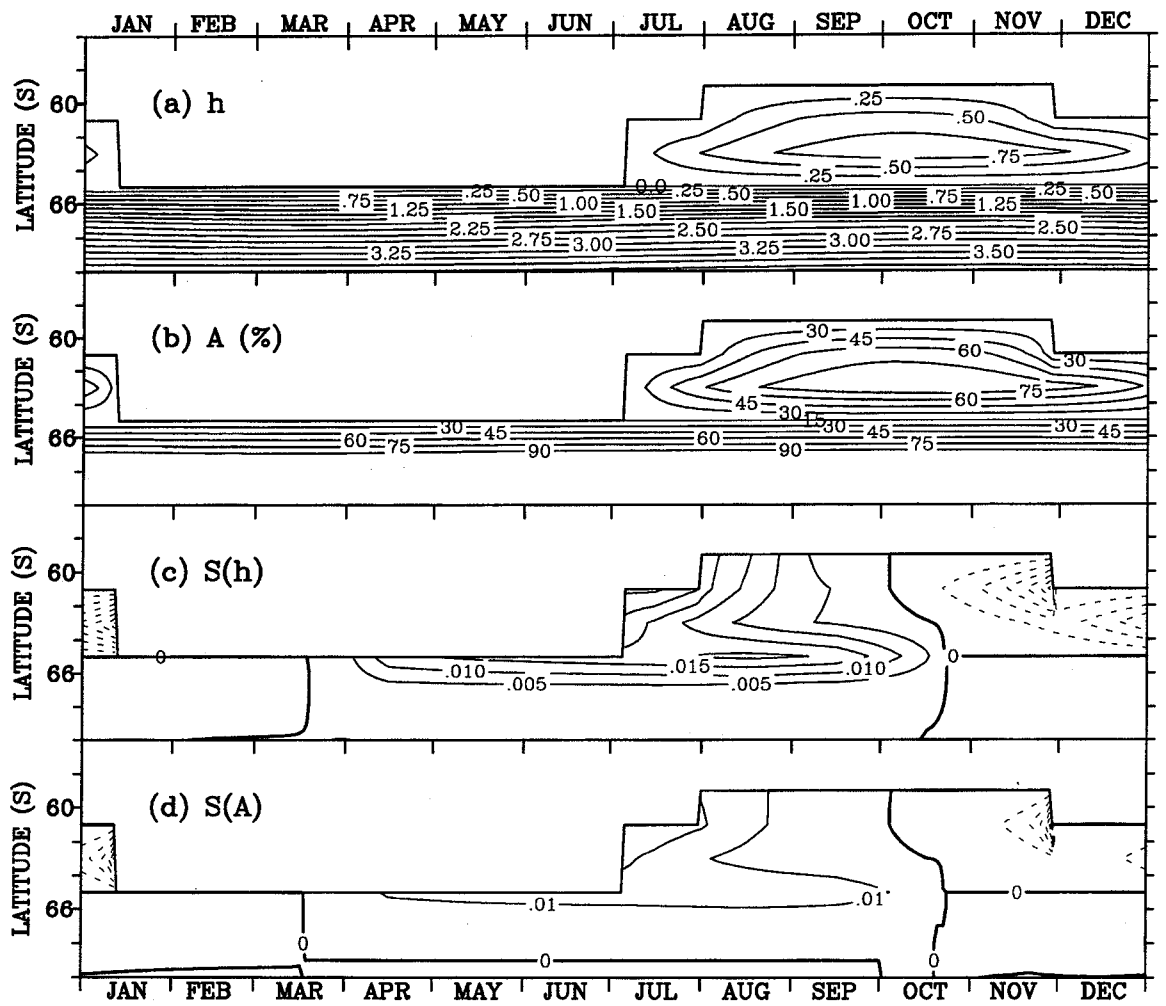

Fig. 7. Distributions of (a) ice thickness, (b) compactness, (c) thermodynamic forcing function S_h for thickness, and (d) thermodynamic forcing function S_A for compactness. These variables are obtained from the thermodynamic-only model with the oceanic heat flux of 6.5 Wm^{-2}, on time and latitude planes during Year 6.

though the part provides the velocity field in the given polynya zone. Fig. 7 shows distributions of ice thickness, compactness, and thermodynamic forcing functions, S_h and S_A, which are obtained from the thermodynamic-only model. There is also the zone of polynya with zero thickness and the minimum compactness of 0.15 (Figs. 7a and 7b). As shown in Figs. 7c and 7d, larger values of the thermodynamic forcing functions are appeared in the same periods as those of the control run with similar magnitudes (Figs. 4c and 5c). With this recognition, we also show distributions of sensible and latent heat fluxes, temperatures on the ice surface, and heat conduction through ice in Fig. 8. Larger values of the four variables are also appeared in the same periods as those of the control run with similar magnitudes shown in Fig. 6. The oceanic heat supplied to the mixed layer and the year that the statistical equilibrium obtained are same for both the full model chosen as the control run and the thermodynamic-only model. Hence, the similarities found in the two model results reconfirm us that thermodynamic forcing functions are dominant in the daily increments excluding the regimes near sea ice edge and the polynya zone.

SUMMARY OF RESULTS AND DISCUSSION

Cavitating fluid sea ice model (Flato and Hibler, 1992) was applied to the Southern Ocean with the Antarctic continent approximated as a circular one. Three modifications were made to the original code. The first was that the calculation of free drift velocity directly from the atmospheric and ocean stresses. The second was that the Coriolis factor changes with latitude. The last was the application of tolerance limit to the consecutive differences of

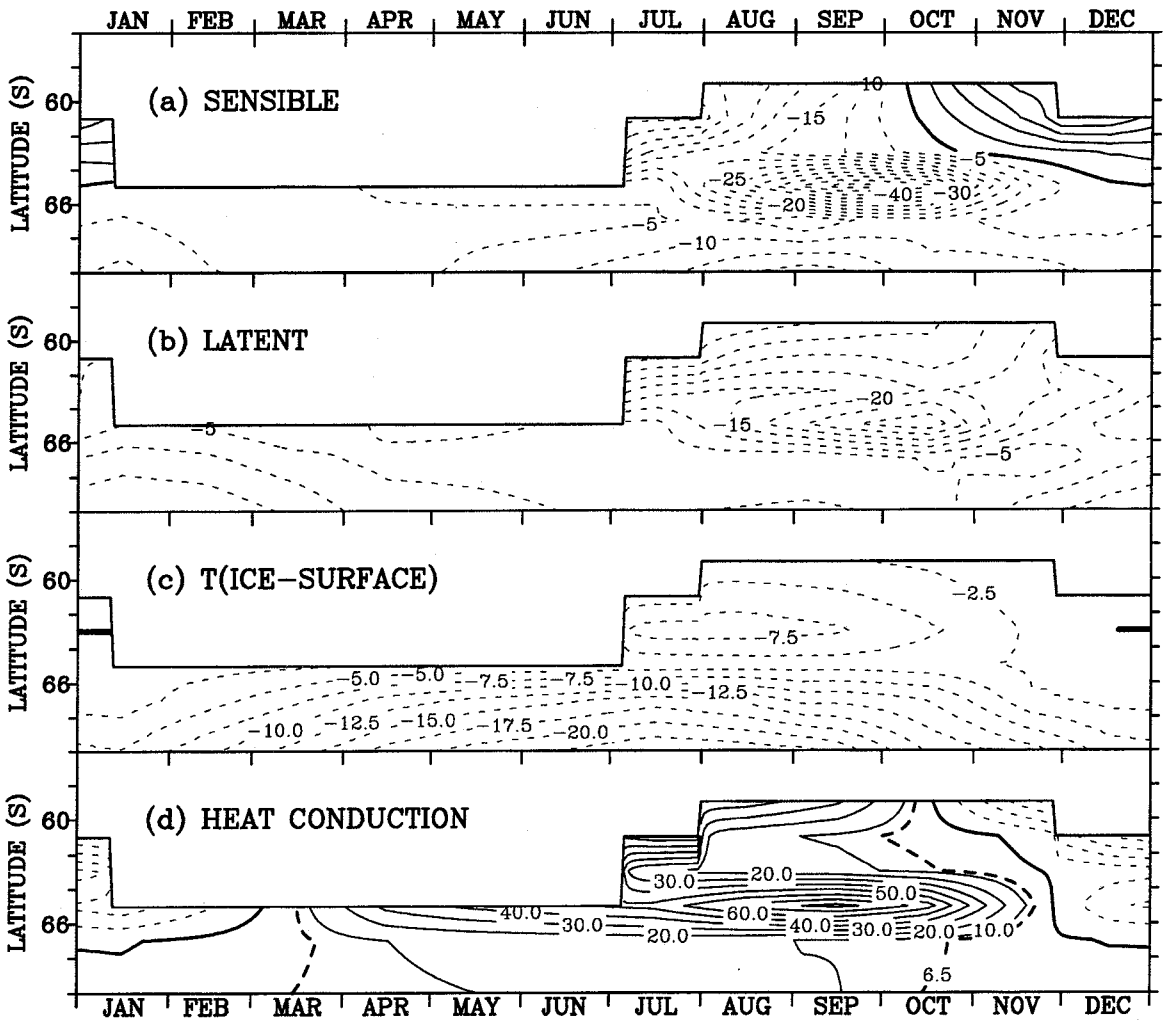

Fig. 8. Same as Fig. 6, except for distributions of variables obtained from the thermodynamic-only model.

ice velocity instead of internal pressure. Forcings were provided using the climatological set of atmospheric fields. There was no forcing from ocean currents included in this study. All model results shown in this paper were symmetric in the zonal direction. The control run results were obtained in the statistical equilibrium state approached in Year 6 with the oceanic heat flux of 6.5 Wm^{-2} supplied to the mixed layer of 60 m thick.

It was confirmed that both the ice velocity and oceanic heat flux were the necessary variable and parameter for the full model to get the ice edge distribution close to the observed. Our results showed that the full model was capable of simulating the free drift in the climatological sense using the coarse model-grids. However, the appearance of polynya zone and overall thermodynamic properties were due to the thermodynamic part of the full model as also proved by the thermodynamic-only model results.

Stoessel *et al.* (1990) showed similar results to ours using a coupled sea ice-mixed layer model. They indicated that sea ice dynamics was essential to describe the pronounced seasonal cycle of ice extent observed in the Southern Ocean. Neglecting sea ice dynamics, the large seasonal extent of sea ice can only be achieved by neglecting mixed-layer dynamics, i.e., adopting the mixed-layer used in this study, and by specifying an unrealistic large constant oceanic heat flux to melt the ice in summer.

Worby and Allison (1991) compiled recent studies of sea ice thickness and concentration in the Southern Ocean. They showed that a much larger area of pack ice is made of young, thin (<0.3 m), first-year ice than previously thought, as appeared in the advanced zone in Fig. 3d.

There appeared seasonal changes of the thermodynamic variables next to the southern boundary (Figs. 4a and 5a). The appearance of thinner and less-compact sea ice during summer season induce positive sensible heat flux from the air to sea ice and negative heat conduction through the ice (Fig. 6). During summer season, the contrast in both the sensible flux and heat conduction might induce a small cell-like structure in the atmosphere. However, during winter season, we could postulate that there would be the internal zone of vertical motion in both the atmosphere and the ocean due to the presence of the polynya zone. Just based on the full model results, another postulation is the possible presence of seasonal heat-pump in the Southern Ocean.

ACKNOWLEDGEMENTS

We are grateful to G. Flato for providing the sea ice code. Thanks to A. Stoessel for his constructive comments on the first version of this paper. Suggestions by two reviewers helped to improve the paper. This research was supported by the Institutional Collaborative Research (INCOR) program, University of California, and by KORDI grant BSPE 97652.

REFERENCES

Ackley, S.F., A.J. Gow, K.R. Buck and K.M. Golden, 1980. Sea ice studies in the Weddell Sea aboard USCGS *Polar Sea*. *Ant. J.U.S.*, **15**: 84–86.

Campbell, W.J., 1965. The wind-driven circulation of ice and water in a polar ocean. *J. Geophys. Res.*, **70**: 3279–3301.

Comiso, J.C. and A.L. Gordon, 1998. Interannual variability in summer sea ice minimum, coastal polynyas and bottom water formation in the Weddell Sea. In: Antarctic Sea Ice: Physical Processes, Interactions and Variability. Antarc. Res. Ser. **74**: 293–315.

Fel'zenbaum, A.I., 1958. The study of steady drift of ice and the calculation of the long period mean drift in the central part of the Arctic Basin. *Problemy Severa*, **2**: 16–46, (English Transl., *Probl. North*, No. 2, 13–44, 1961).

Flato, G.M. and W.D. Hibler III, 1992. Modeling pack ice as a cavitating fluid. *J. Phys. Oceanogr.*, **22**: 626–621.

Gloersen, P., W.J. Campbell, D.J. Cavalieri, J.C. Comiso, C.L. Parkinson and H.J. Zwally, 1992. Arctic and Antarctic Sea Ice, 1978–1987: Satellite Passive-Microwave Observations and Analysis. NASA SP-511, Scientific and Technical Information Program, National Aeronautics and Space Administration, Washington, D.C., 290 pp.

Gordon, A.L., 1981. Seasonality of Southern Ocean sea ice. *J. Geophys. Res.*, **86**: 4193–4197.

Hibler, W.D., III, 1979. A dynamic thermodynamic sea ice model. *J. Phys. Oceanogr.*, **9**: 815–846.

Hibler, W.D., III, 1980. Modeling a variable thickness sea ice cover. *Mon. Wea. Rev.*, **108**: 1943–1973.

Hyde, W.T., K.-Y. Kim, T.J. Crowley and G.R. North, 1990. On the relation between polar continentality and climate: studies with a nonlinear seasonal energy balance model. *J. Geophys. Res.*, **95**: 18653–18668.

Jenne, R.L., H.L. Crutcher, H. Van Loon and J.J. Taljaard, 1971. Climate of the Upper Air. Southern hemisphere, III: Vector Mean Geostrophic Winds, Isogon and Isotach Analyses. NCAR-TN/STR-58, Nat. Center for Atmos. Res., Boulder, Colo.

Kottmeier, C., J. Olf, W. Frieden and R. Roth, 1992. Wind forcing and ice motion in the Weddell Sea region. *J. Geophys. Res.*, **97**: 20373–20383.

Kottmeier, C. and L. Sellmann, 1996. Atmospheric and oceanic forcing of Weddell Sea ice motion. *J. Geophys. Res.*, **101**: 20809–20824.

Lemke, P., W.D. Hibler, G. Flato, M. Harder and M. Kreyscher, 1997. On the improvement of sea ice models for climate simulations: the Sea Ice Model Intercomparison Project. *Ann. Glaciol.*, **25**: 183–187.

McPhee, M.G., 1975. Ice-ocean momentum transfer for the AIDJEX ice model. *AIDJEX Bull.*, **29**: 93–111.

Martinson, D.G. and Wamser, 1990. Ice drift and momentum exchange in winter Antarctic pack ice. *J. Geophys. Res.*, **95**: 1741–1755.

Maykut, G.A. and N. Untersteiner, 1971. Some results from a time-dependent, thermodynamic model of sea ice. *J. Geophys. Res.*, **76**: 1550–1575.

Meehl, G.A., 1992. Global coupled models: atmosphere, ocean, sea ice. In: Climate System Modeling, edited by Trenberth, K.E., Cambridge University Press, New York, pp. 555–581.

Parkinson, C.L. and W. Washington, 1979. A large-scale numerical model of sea ice. *J. Geophys. Res.*, **84**: 311–337.

Rothrock, D.A., 1975. The steady drift of an incompressible Arctic ice cover. *J. Geophys. Res.*, **80**: 387–397.

Sasamori, T., J. London and D.V. Hoyt, 1972. Radiation budget of the Southern Hemisphere. In: Meteorology of the Southern Hemisphere, vol. 13, American Meteorological Society, Boston, pp. 9–23.

Semtner, A.J., Jr., 1976. A model for the thermodynamic growth of sea ice in numerical investigation of climate. *J. Phys. Oceanogr.*, **6**: 379–389.

Semtner, Jr., A.J. and R.M. Chervin, 1992. Ocean general circulation from a global eddy-resolving model. *J. Geophys. Res.*, **97**: 5493–5550.

Stoessel, A., P. Lemke and W.B. Owens, 1990. Coupled sea ice-mixed layer simulations for the Southern Ocean. *J. Geophys. Res.*, **95**: 9539–9555.

Taljaard, J.J., H. Van Loon, H.L. Crutcher and R.L. Jenne, 1969. Climate of the Upper Air I. Southern Hemisphere, Vol. 1, Temperatures, Dew Points and Heights at Selected Pressure Levels. NAVAIR Rep. 50-1C-55, U.S. Nav. Weather Serv. Command, Washington, D.C., 135 pp.

Vihma, T. and J. Launiainen. 1993. Ice drift in the Weddell Sea in 1990-1991 as tracked by a satellite buoy. *J. Geophys. Res.*, **98**: 14471–14458.

Worby, A.P. and I. Allison, 1991. Ocean-atmosphere energy exchange over thin, variable concentration Antarctic pack ice. *Ann. Glaciol.*, **15**: 184–190.

Zwally, H.J., C. Parkinson, F. Carsey, P. Gloerson, W.J. Campbell and R.O. Ramseier, 1979. Antarctic sea ice variations 1973–1975. In: NASA Weather Climate Review, Pap. 56, National Aeronautics and Space Administration, Washington, D.C., pp. 335–340.

Zwally, H.J., C. Comiso, C.L. Parkinson, W.J. Campbell, F.D. Carsy and P. Gloeson, 1983. Antarctic Sea Ice, 1973–1976: Satellite Passive-Microwave Observations, NASA Spec. Publ., SP-459, 206 pp.

Manuscript received October 31, 1998
Revision accepted March 20, 1999